Selective dehydration of glycerol on copper based catalysts

Chimentão, R. J.; Hirunsit, P.; Torres, C. S.; Ordoño, M. Borges; Urakawa, A.; Fierro, J. L.G.; Ruiz, D.

Important note
To cite this publication, please use the final published version (if applicable).
Please check the document version above.

Selective dehydration of glycerol on copper based catalysts

R. J. Chimentão[1,§,*], P. Hirunsit[2,§], C. S. Torres[1], M. Borges Ordoño[3], A. Urakawa[3,4],

J.L.G. Fierro[5], D. Ruiz[1]

[1] *Universidad de Concepción, Facultad de Ciencias Químicas, Edmundo Larenas 129,*

Casilla 160C, Chile

[2] *National Nanotechnology Center (NANOTEC), National Science and Technology*

Development Agency (NSTDA), Pathum Thani, 12120 Thailand

[3] *Institute of Chemical Research of Catalonia (ICIQ), The Barcelona Institute of Science*

and Technology, Av. Països Catalans 16, 43007 Tarragona, Spain

[4] *Catalysis Engineering, Department of Chemical Engineering, Delft University of*

Technology, Van der Maasweg 9, 2629 HZ Delft, The Netherlands

[5] *Institute of Catalysis and Petrochemistry (CSIC), Cantoblanco, 28049, Madrid, Spain*

§ These authors contributed equally

* Corresponding author: *rchimenton@udec.cl*

Phone number: +56 (041) 220-3354

Abstract

Glycerol is produced in large quantities as a byproduct of biodiesel, and among others hydroxyacetone (acetol) is an important commodity obtained from glycerol. Metallic Cu has been identified as active site for the dehydration of glycerol to hydroxyacetone and acid and metal sites are known to influence the catalytic performance.

In this study, dehydration of glycerol over 5 wt.% copper supported on γ-Al_2O_3, ZrO_2 and SiO_2 was investigated. Catalysts were characterized by N_2 physisorption, H_2-TPR, NH_3-TPD, N_2O chemisorption, XPS, XRD, FTIR of pyridine adsorption. Cu/ZrO_2 exhibited the highest hydroxyacetone yield at 20% of glycerol conversion and the highest apparent reaction rate. The superior activity of Cu/ZrO_2 was attributed to the highly acidic, both Lewis and Brönsted acidic, nature of the support and positive roles of the interfacial sites. The Weisz-Prater (WP) criterion was applied to confirm the absence of intraparticle diffusion limitations. It was assumed spherical particles and first order reaction. The WP value obtained in the worst scenario was less than 0.3 ensuring no diffusion limitation.

Complementary DFT study indicates that both glycerol and hydroxyacetone interact significantly stronger on Cu/γ-Al_2O_3 and Cu/ZrO_2 compared to metallic Cu, suggesting that the active sites are at the interface of Cu particles and the acidic support.

Key-words: Glycerol, Dehydration, Hydroxyacetone, Copper, Catalyst

1. Introduction

Glycerol is a relevant bio-renewable compound for its increasing availability, since it is produced in large quantities as a by-product during the transesterification of ester to obtain biodiesel. The glycerol produced represents 10% of the total mass of the biodiesel production. Glycerol is a compound of great importance already in our daily lives, e.g. in food industry, due to its non-toxic nature [2], and it could become one of the most important building blocks for chemical production in the biorefinery [1]. Related to the latter, a variety of catalytic conversion routes to valorise the molecule, such as hydrogenolysis to propylene glycol [3], catalytic reforming [4], cracking for the production of olefins and light parafins [5], oxidation towards acids (dihydroxyacetone, tartronic acid, glyceric acid) [6], oligomerization, polymerization towards glycerol monoesters [7], transesterification to monoglycerides [8], dehydration to acrolein or hydroxyacetone [9], carboxylation to glycerol carbonate [10], have been reported to date.

This work focuses on the selective dehydration of glycerol to hydroxyacetone. Hydroxyacetone is an interesting building block due to its extremely reactive multifunctional structure which contains hydroxyl and carbonyl functional groups. Particularly, it is an attractive intermediate of 1,2-propanediol (1,2-PDO) which is used for the synthesis of resins, liquid detergents, cosmetics, and pharmaceuticals and can be produced by hydrogenation of hydroxyacetone. 1,2-PDO is currently produced from fossil fuel derived propylene oxide. The catalytic process for the conversion of glycerol to 1,2-PDO requires external hydrogen supply. The use of external H_2 has a negative impact to the process. Direct dehydration of glycerol would form hydroxyacetone molecule without the need for hydrogen consumption

and under moderate conditions. Thus, the synthesis of 1,2-PDO from glycerol-derived hydroxyacetone offers a greener production method of 1,2-PDO and is one of the attractive paths for glycerol valorisation [3]. In addition, since hydroxyacetone is a highly reactive molecule, it can be used as an intermediate in organic synthesis to produce other compounds such as propionaldehyde, acetone and furan derivatives. Hydroxyacetone is a compound that lacks toxicity, which justifies its use in the textile, pharmaceutical and food industries. Furthermore , hydroxyacetone stands out as a key reagent for the production of lactic acid which has acquired significant interest since it is considered one of the 12 best molecules of the biological-based platform due to its wide potential applications in pharmaceutical and food industry or as biodegradable plastics among others [11].

Conventionally, hydroxyacetone has been synthesized by several ways: (i) reaction of bromoacetone with sodium or potassium formate (or acetate) followed by hydrolysis of the ester with methyl alcohol; (ii) direct oxidation of acetone with the Bayer-Villeger reagent [12]; (iii) dehydrogenation of aqueous propylene glycol in the presence of palladium-catalyzed hydrogen peroxide [13]; (iv) biosynthetic pathway which involves metabolically manipulated microorganisms using various substrates [14]. However, the presence of multi-step reagents in stoichiometric quantities, the low yields and the effluent disposal costs restrict the commercialization of any of these methods, thus the production of hydroxyacetone from inexpensive and often-wasted bio-glycerol is beneficial for environmental protection [9].

Sato *et al.* [15] investigated the dehydration of glycerol in the gas phase to hydroxyacetone over Ag catalysts achieving 91% conversion of glycerol with 86% selectivity to hydroxyacetone at 240°C under H_2 flow, however strong catalyst deactivation was observed. Chiu *et al.* [16] studied the conversion of glycerol in gas phase to hydroxyacetone in a high-pressure and high temperature semi-continuous reactor by reactive distillation over copper chromite catalyst. They observed 22% glycerol conversion and 70% hydroxyacetone selectivity. However, the toxicity associated to the Cr species in these catalysts and the deactivation due to coke formation requires further catalyst development. It has been reported that acidic sites have an important role in the glycerol dehydration and they can modulate the yield towards hydroxyacetone. The presence of Brönsted acid sites is reported to favor the dehydration of glycerol to acrolein, whereas Lewis acid sites promote the selective formation of hydroxyacetone [17].

Copper is recognized for its intrinsic ability to break preferentially the C-O primary bond of alcohols [18]. It is also suggested that copper oxide species act as Lewis acid sites to polarize the C-O bond of glycerol [19]. This property of copper is of vital importance for obtaining hydroxyacetone since this molecule is obtained by dehydration of any primary hydroxyl group of glycerol. The support material is known to participate directly on the selective dehydration. According to Sato *et al.* [1] the combination of an acid oxide support such as Al_2O_3 to copper effectively promotes the selectivity to hydroxyacetone in the glycerol conversion. This indicates that not only the copper species play an important role in the dehydration but the Lewis acid sites of the support are also important for the formation of hydroxyacetone. R. Mane *et al.* [9] investigated Cu-Al catalysts prepared by co-precipitation

111   and 24% glycerol conversion and 92% hydroxyacetone selectivity in the liquid phase were

112   observed with an aqueous solution of 20 wt.% of glycerol, 220 °C and in a N_2 atmosphere.

113

114   In addition, P. Hirunsit *et al.* [20] have reported selectivity higher than 90% towards 1,2-

115   PDO with copper catalysts supported on Al_2O_3. A. Bienholz *et al.* [21] reported for Cu/SiO_2

116   catalysts prepared by ammonia evaporation, 92% glycerol conversion and 69% selectivity to

117   hydroxyacetone in gas phase with an aqueous solution of 40 wt.% glycerol in a H_2

118   atmosphere in a fixed bed reactor. It should be added that Dasari *et al.* [3] have reported that

119   Raney copper has shown in the glycerol hydrogenolysis 69% selectivity towards 1,2-PDO

120   with 49% conversion at 200°C and H_2 pressure of 14 atm.

121

122   The results outlined above may indicate that copper alone can catalyze glycerol dehydration

123   and the support may facilitate copper species to be more active in the dehydration of glycerol.

124   The present work focuses on the study of the selective dehydration of glycerol towards

125   hydroxyacetone in aqueous phase on copper catalysts supported on materials with different

126   nature of acid properties. Particularly in the present work it will be studied the effect of the

127   total amount of acid sites; dispersion of copper species and the effect of three different

128   supports (SiO_2, γ-Al_2O_3 and ZrO_2) in the selective dehydration of glycerol to hydroxyacetone.

2. Experimental

2.1 Catalyst preparation

Cu/γ-Al$_2$O$_3$ and Cu/ZrO$_2$ catalysts were prepared by incipient impregnation with a 5% mass content of copper with respect to the weight of the support. The metal precursor was an aqueous solution of Cu(NO$_3$)$_2$·3H$_2$O. After the impregnation step, the samples were kept under hood at room temperature for 4 hours and finally dried at 120 °C for 24 hours. Once dried they were calcined in a muffle with a heating ramp of 5 °C min^{-1} from room temperature to 400 °C for 4 hours. Cu/SiO$_2$ catalyst was prepared by ammonia evaporation method [22] with a mass content of 5% of copper relative to the support. Briefly 25 wt.% ammonia solution was added in an aqueous solution of Cu(NO$_3$)$_2$·3H$_2$O under vigorous stirring until it reached pH 12. The resulting solution was heated to 80 °C maintaining this temperature until it reached a pH of 6.0-7.0. The final product was filtered and washed with water, followed by drying at 120 °C for 24 hours. It was then calcined in a muffle furnace with a heating ramp of 5°C min^{-1} from room temperature to 400 °C for 4 hours. Finally, prior to the reaction the catalysts were reduced in a quartz reactor under H$_2$ flow at 50 mL min^{-1} from room temperature to 400 °C with a heating ramp of 5 °C min^{-1} and then they were kept at 400 °C for 4 hours.

2.2 Catalyst Characterization

The specific surface areas of the copper-based catalysts were measured with a Micromeritics ASAP 2010 physisorption apparatus with N$_2$ at 77 K. BET and BJH methods were used respectively for the calculation of the surface areas and pore characteristics (size distribution

151   and volume). Prior to the analysis, the samples (about 100 mg) were degassed for 4 hours at

152   120 ° C using N_2 as a carrier gas.

153   X-ray powder diffraction (XRD) measurements were conducted on a Bruker X-ray

154   diffractometer model D4 Endeavor (Kα Cu, 40 kV and 20 mA) operating with 2θ range of

155   20 - 90° at a scanning rate of 0.02° for 0.3 s.

156   FTIR spectra were collected using a FTIR-Vertex 70V instrument (Bruker) equipped with a

157   Harrick cell TM (powder, ca. 30 mg). Prior to pyridine adsorption experiments, the samples

158   were pre-treated at 400°C for 1 hour in hydrogen flow. The system was then cooled down to

159   reach 150 °C under helium flow. Pyridine vapor adsorption was performed at 150 °C (30

160   spectra, 1 spectrum per minute). Finally, pyridine desorption was monitored for 1 hour under

161   He flow at 150 °C from temperature ramping up (from 150 to 400 °C). Background spectra

162   were collected before pyridine adsorption.

163   Temperature programmed desorption of NH_3 (NH_3-TPD) experiments were performed in a

164   Micromeritics AutoChem II 2920 automatic equipment. Prior to the experiments, the

165   catalysts (about 100 mg) were reduced at 400 °C for 120 min in 10% H_2/Ar at 20 mL min^{-1},

166   and after the reduction samples were cooled to 35 °C under the same flow. Then catalysts

167   were treated with NH_3 (20 mL min^{-1}) for 10 min at 40 °C. Thus, the samples were treated in

168   He flow (50 mL/min) to purge the system. Finally, the NH_3 desorption was carried out by

169   heating the reactor with a temperature ramp of 5 °C min^{-1} in a flow of He (20 mL min^{-1}). A

170   trap of water, ice and NaCl salt was used. The NH_3 consumption has been determined by a

171   thermal conductivity detector (TCD).

172 The amount of surface copper atoms was measured on the samples (about 100 mg) initially

173 reduced in hydrogen flow of 50 mL min^{-1} at 400 °C. The reduced samples were cooled in He

174 flow (50 mL/min) to 60 °C and purged for 30 minutes. 20% N_2O/Ar gas was added for

175 1 hour. The selective oxidation of the copper surface to Cu_2O was performed under 20%

176 N_2O/Ar flow (50 mL min^{-1}) at 60 °C:

177

178 $N_2O + 2Cu_{surface} \rightarrow Cu_2O_{surface} + N_2$ (1)

179

180 The system was then cooled to room temperature in He flow (50 mL min^{-1}) to eliminate the

181 physisorbed species of N_2O. $Cu_2O_{surface}$ was further reduced with 5% H_2/Ar flow (50 mL min^{-1}

182 ^{1}) by raising the temperature at 5 °C min^{-1} from room temperature to 900 °C. The H_2

183 consumption was followed by TCD detector.

184

185 $H_2 + Cu_2O_{surface} \rightarrow 2Cu_{surface} + H_2O$ (2)

186

187 VG Escalab 200R spectrometer equipped with a hemispherical electron analyser and an Mg

188 Kα (hν=1253.6 eV, 1 eV=1.603 ×10^{-19} J) was employed for X-ray photoelectron

189 spectroscopy (XPS) measurements. The X-ray source operated at 10 mA and 12 kV. The

190 spectrometer chamber pressure during data acquisition was maintained at 1×10^{-7} Pa. The

191 peaks were fitted by a non-linear least square fitting program using a properly weighted sum

192 of Lorentzian and Gaussian component curves after background subtraction. The constant

193 charging of the samples was corrected by referencing all energies to the Al 2p peak at

194 74.5 eV.

195   *2.3 Catalytic Activity*

196   Dehydration of glycerol was studied in a 300 mL batch reactor with a content of 60 mL of

197   reaction mixture with an aqueous solution of 80 wt.% of glycerol, 500 mg of catalyst which

198   corresponds to a glycerol/Cu molar ratio of 1000. The reaction was carried out for 3 hours

199   under a constant stirring of 800 rpm and temperature of 190 °C. The reaction was performed

200   under N_2 atmosphere.

201   The reaction products were analysed at different reaction time by an autosystem XL gas

202   chromatograph equipped with an FID detector and Nukol Capillary column (30 m long, 0.53

203   mm internal diameter and 0.5 μm film space) with He as a carrier gas. The products were

204   also analysed with a gas chromatograph coupled to a mass spectrometer. The glycerol

205   conversion and product selectivity were calculated according to:

206
$$Conversion\ (\%) = \frac{(moles\ of\ glycerol\ reacted)}{(initial\ moles\ of\ glycerol)} \times 100 \qquad (3)$$

207

208
$$Product\ i\ selectivity\ (\%) = \frac{(moles\ of\ C\ in\ the\ product\ i)}{(moles\ of\ C\ in\ the\ initial\ quantity\ of\ glycerol)} \times 100$$

209   (4)

210   To ensure the absence of intra-particle diffusion resistance the Weisz-Prater (WP) parameter

211   was calculated. According to WP criteria, if WP (φ) ≤ 0.3 the internal diffusion resistance

212   can be neglected for a heterogeneous reaction. Where φ is:

213
$$\varphi = \frac{-r_{obs}\rho_c R_p{}^2}{D_e C_{AS}} \qquad (5)$$

214

215 Where, $-r_{obs}$ = the observed rate (molg$_{cat}^{-1}$s^{-1}), ρ_c = solid catalyst density =2.08 g.cm^{-3}, R_P=

216 catalyst particle radius = 0.0025 cm, C_{AS} = concentration of glycerol at catalyst surface =

217 0,001 mol cm^{-3}. D_e is the effective diffusivity of glycerol to water (2.11 x 10^{-5} cm^2 s^{-1}) and:

$$D_e = \frac{D_{AB}\phi\sigma}{\tau} \qquad (6)$$

219 Where ϕ = porosity pellet = 0.42, σ = constriction factor = 0.8 and τ = tortuosity = 3 [23, 24]

220 and D_{AB} = diffusion coefficient of glycerol to water at 250 °C = 1.85×10^{-4} cm^{2}s^{-1} calculated

221 by Wilke-Chang Equation:

$$D_{AB} = \frac{1.173\times10^{-13}(\phi M_B)^{0.5}T}{\mu V_A{}^{0.6}} \qquad (7)$$

223 Where ϕ is the factor for solute-solvent interaction; Temperature (K); V_A = molar volume of

224 solute at boiling point (glycerol), M_B = molecular weight of solvent (water) and μ is the

225 solvent viscosity.

226

227 Finally $-r_{obs}$ is:

$$-r_{obs} = \frac{n}{V\times m_{cat}\times t} \qquad (8)$$

229 Where n = moles of glycerol reacted, V = volume in L, m_{cat} = catalyst weight in g and t =

230 reaction time in minutes.

231

232 *2.4 Computational Details*

233 The Cu(111) surface model was constructed with a supercell of 4×4 containing 4 layers of

234 metal atoms and a vacuum region ~15 Å. The two atomic layers from the bottom of the slab

235 were fixed, while the top two layers were relaxed to their lowest energy configurations. The

236 fixed layers were set to Cu bulk bond distances according to the optimized lattice constant

11

237   that was determined from bulk calculation. The slab model of γ-Al$_2$O$_3$(110) surface contains

238   thirty two Al$_2$O$_3$ molecular units and ~15 Å of the vacuum region. The (110) crystalline

239   surface was chosen because it dominates in γ-alumina nanocrystallites (~70-83% of total

240   area) [25, 26]. Twelve of Al$_2$O$_3$ molecular units located in atomic layers from bottom of the

241   slab were fixed and the rest were relaxed including the Cu$_{13}$ cluster and adsorbates. The fixed

242   layers were set to γ-Al$_2$O$_3$ bulk bond distances in which the γ-Al$_2$O$_3$ bulk model structure was

243   taken from references [25, 27]. The tetragonal ZrO$_2$ bulk structure was applied followed the

244   experimental observation. The slab model of most stable ZrO$_2$(111) surface was modeled

245   with total thirty nine molecular units and ~15 Å of the vacuum region excluding adsorbates.

246   Seventeen ZrO$_2$ molecular units from the bottom of a slab were fixed and the rest were

247   relaxed including Cu$_{13}$ cluster and adsorbates. The structures of bare Cu(111), Cu$_{13}$/γ-

248   Al$_2$O$_3$(110) and Cu$_{13}$/ZrO$_2$(111) are shown in Fig. S5 of supporting information.

249   The initial geometries of isolated Cu$_{13}$ cluster were modeled based on the possible M$_{13}$

250   nanoparticle structures reported in previous studies [28, 29]; icosahedral (ICO), face centered

251   cubic (FCC), hexagonal close packed (HCP), capped cubic (CC), buckled biplanar (BBP),

252   triangular biplanar (TBP), and cage-like (CAG). The two most stable structures of isolated

253   Cu$_{13}$ cluster structures were found to be ICO and BBP (Fig. S4 of supporting information).

254   Then, the optimized ICO and BBP Cu$_{13}$ clusters were initially placed on the γ-Al$_2$O$_3$(110)

255   and ZrO$_2$(111) surfaces with variations of location on the surfaces and orientations of the

256   Cu$_{13}$ clusters. The most stable structures found for Cu$_{13}$/Al$_2$O$_3$(110) and Cu$_{13}$/ZrO$_2$(111) (Fig.

257   S5 of supporting information) were then applied for glycerol and hydroxyacetone adsorption

258   study. The 13-atom Cu cluster model can represent small particle size (~ 1nm) which has an

259   average number of metal atoms in the range 11-14 atoms. The models present Cu-Cu and

260   Cu-support interaction. Cu_{13} cluster were widely applied to study catalytic reaction such as

261   CO oxidation and ammonia decomposition [30-32]. It should be noted that the copper particle

262   size and shape can affect the reactivity as well which may be due to the variation of the

263   amount of low coordinated defect sites. The supported metal-13 cluster on support such as γ-

264   Al_2O_3 surface also were previously employed to study NO oxidation [33], H_2 dissociation

265   [34], the nature of the metal-support interaction [35], and stability of clusters on support [36].

266   Hydroxyl are created and adsorbed on Al_2O_3 and ZrO_2 surfaces due to the adsorption of water

267   which is a product of glycerol dehydration [25, 37]. The effect of hydroxylation on the

268   supports were also investigated. The relationship between the hydroxyl coverage on γ-

269    $Al_2O_3(110)$ surface and temperature has been investigated previously by Digne *et al.*[25]

270   Applying this relationship, the OH coverage on γ-$Al_2O_3(110)$ surface corresponding to the

271   experimental temperature in the range of 130-230 $^{\circ}$C is approximately 3.0-11.8 OH nm^{-2}.

272   The approximately 4.5 OH nm^{-2} coverage corresponding to 4 H_2O molecules on the γ-

273    $Al_2O_3(110)$ and $ZrO_2(111)$ surfaces were employed in this work. The hydroxyl group

274   adsorption was particularly located nearby the copper cluster model in order to bring in the

275   effect of hydroxylation on the dual roles of support and copper cluster.

276   The Vienna *ab initio* Simulation Program [38, 39] was employed to perform fully periodic

277   plane-wave density functional theory (DFT) calculations. Spin-polarized DFT calculations

278   were performed using the GGA-PBE functional [40] implemented with the Projector

279   Augmented Wavefuction (PAW) [41, 42] method for representing the non-valence core

280   electrons. The long-range dispersion force was included using the semi empirical dispersion

281   potential correction method described by Grimme and coworkers [43, 44]. The plane-wave

282   energy cutoff was optimized at 450 eV. The Gaussian broadening [45] with a smearing width

283   of 0.1 eV was employed. The dipole correction was included only in z direction and the

284   surface Brillouin zone was sampled with a 2×2×1 Monkhorst-Pack k-point mesh [46] for all

285   surface calculations. The results were checked for convergence with respect to energy cutoff

286   and number of k-points. The convergence criterion for electronic self-consistent iteration was

287   set to 10^{-7} eV and the ionic relaxation loop was limited for all forces smaller than 0.030 eV

288    $Å^{-1}$ for free atoms. Bader charge analysis was performed using VASP-VTST [47–49].

289

290   **3. Results**

291   *3.1 Catalyst characterization*

292   The textural properties of the supports and copper catalysts are summarized in Table 1 and

293   Fig. 1. Specific area (S_{BET}), pore volume (V_{pore}) and pore diameter (d_{pore}) of the catalysts

294   decrease compared to their supports due to the introduction of copper, indicating a partial

295   blockage of the pores. ZrO_2 and SiO_2 exhibited the smallest and the highest specific surface

296   area, respectively.

297

298   Table 1. Textural parameters of supports and copper catalysts.

299

Sample	S_{BET} ($m^2\ g^{-1}$)	V_{Pore} ($cm^3\ g^{-1}$)	d_{pore} (nm)
ZrO_2	146	0.17	4.3
$γ$-Al_2O_3	212	0.39	7.4
SiO_2	319	0.85	10.6
5% Cu/ZrO_2	131	0.13	4.0
5% Cu/$γ$-Al_2O_3	181	0.34	7.5
5% Cu/SiO_2	244	0.70	11.6

306

307   Fig. 1a shows N_2 sorption isotherms of the supports and Cu catalysts. Isotherms displayed a

308   type-IV curves characteristic of mesoporous structure [50]. For SiO_2-based materials a H1-

309   type hysteresis loop corresponding to uniform spherical pores from a regular matrix of pore

310   size distribution centered at 10-12 nm (Fig. 1b) was found. For materials based on γ-Al_2O_3

311   and ZrO_2 a H2-type hysteresis loop and pore size distribution centered at 4 and 7 nm were

312   found, respectively.
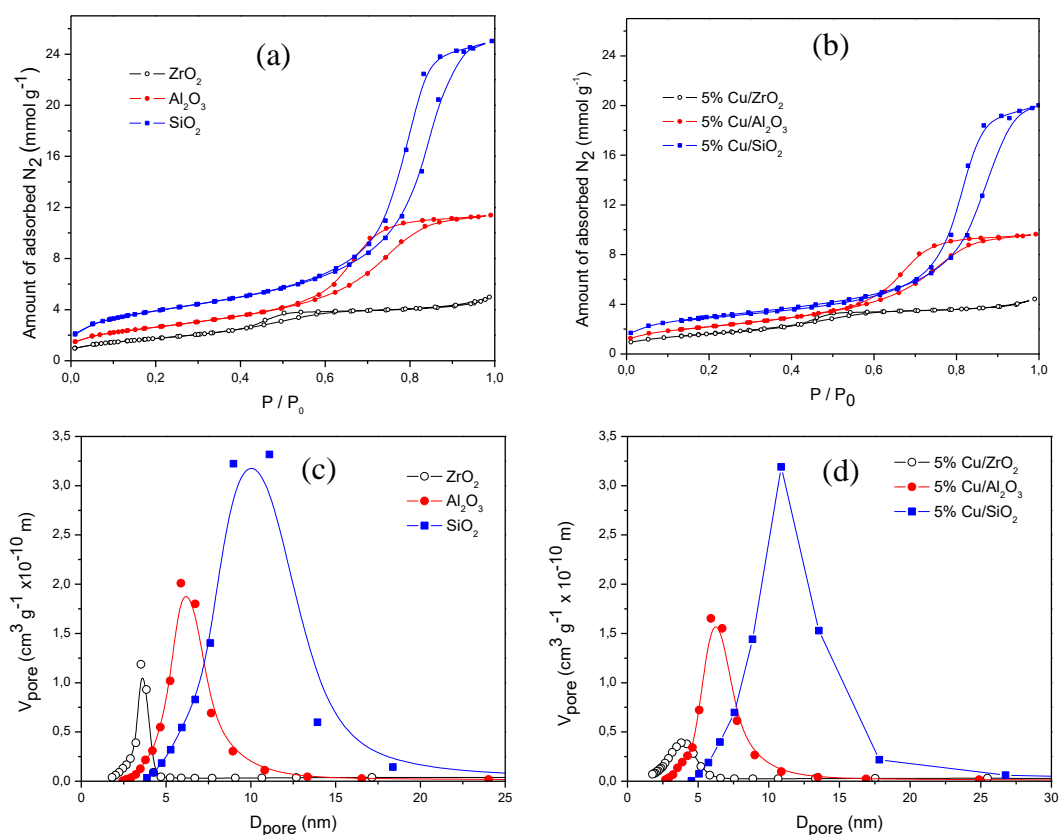
313

314   Fig. 1. (a) and (b) N_2 adsorption-desorption at 77 K and (c) and (d) Pore size distribution.

315

316   By XRD, diffraction peaks only due to the support materials (Fig. 2) were found for all

317   samples. Copper species are expected to exhibit reflection peaks as follows: metallic copper

318   (Cu^0) at 2θ = 43, 50 and 74 ° (JCPDS 04-0836), copper (II) oxide (CuO) at 2θ = 32.6, 35.6,

319   38.6, 48.8, 53.6, 58.3, 61.6, 66.4, 68.1, 72.3 and 75.1 ° (JCPDS 48-1548) and copper (I) oxide

320   (cuprous oxide, Cu_2O) at $2\theta = 36.4$, 42.3 and 61.3 ° (JCPDS 05-0667). The absence of the

321   reflection peaks due to copper species indicates their high dispersion. At 7 wt.% of copper it

322   is reported to be possible to identify Cu peaks in the XRD analysis [51]. Previous work

323   reported that the highly crystalline CuO is formed from approximately 4 wt.% of Cu for 100

324    $m^2 g^{-1}$ of γ-Al_2O_3 [52].

325

326
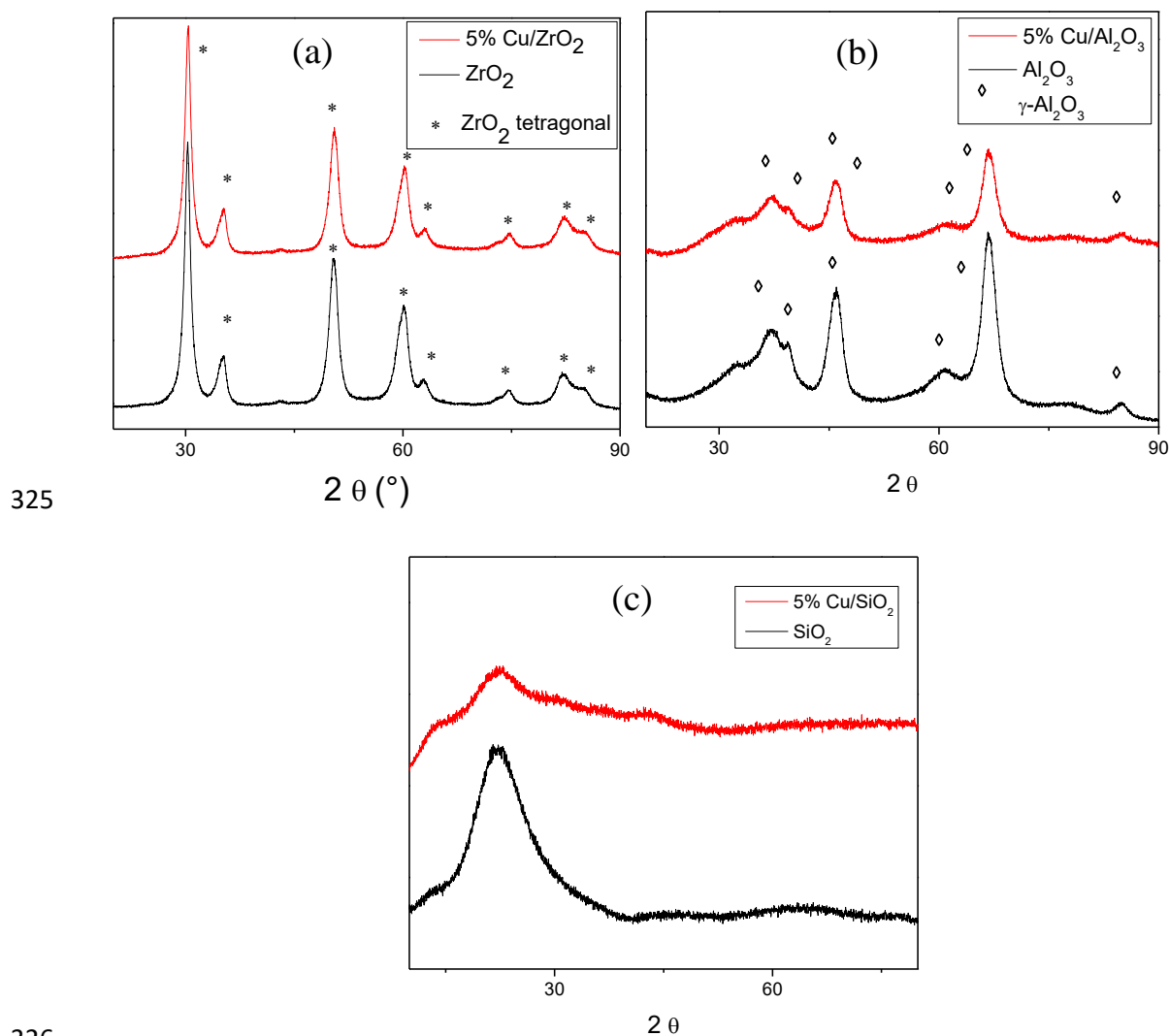
327   Fig. 2. Powder XRD patterns of (a) ZrO_2 (b) γ-Al_2O_3 and (c) SiO_2 materials.

328

329 Only tetragonal zirconia (no monoclinic) patterns were observed in ZrO_2-based materials

330 (Table 2). For the materials based on γ-Al_2O_3 the presence of characteristic peaks of the

331 support (JCPDS 029-0063) was observed at 2θ = 31.9, 37.6, 39.5, 45.8, and 66.7°. X-ray

332 diffraction reveals the amorphous nature of SiO_2.

333

334 Table 2. XRD pattern of monoclinic (JCPDS 37-1484) and tetragonal ZrO_2 (JCPDS 17-

335 0923).

Monoclinic ZrO_2		Tetragonal ZrO_2	
2θ (°)	Crystallographic plane	2θ (°)	Crystallographic plane
24.2	(0,1,1)	30.1	(1,1,1)
28.2	(1,1,0)	35.2	(2,0,0)
31.4	(0,2,0)	50.4	(2,2,0)
34.3	(1,2,1)	59.9	(3,1,1)

336

337 The evaluation of acidity of the support and catalyst materials by NH_3-TPD (Table 3 and Fig.

338 3) showed an increase of the total acidity for the catalysts containing copper species. Cu/ZrO_2

339 has the highest acidity (867 µmol g_{cat}^{-1}) in contrast to Cu/SiO_2 that presented the lowest total

340 amount of acid sites (187 µmol g_{cat}^{-1}).

341 Table 3. Quantitative analysis of NH_3-TPD data of ZrO_2, γ-Al_2O_3 and Cu-based catalysts.

Sample	Total NH_3 amount	
	(µmol g_{cat}^{-1})	(µmol m^{-2})
ZrO_2	360	-----
γ-Al_2O_3	280	-----
5% Cu/ZrO_2	867	6.6
5% Cu/Al_2O_3	591	3.3
5% Cu/SiO_2	187	0.8

342

ZrO$_2$ support showed a signal with a maximum at 270 °C and a tail-like broad desorption

extending to approximately 630 °C, indicating a wide distribution of the strength of the acid

sites ranging from moderate (considered from 200-450 °C) to strong (> 450 °C) ones. The

Cu/ZrO$_2$ catalyst also exhibited a wide distribution of acid sites with different acid strengths

and the total amount of acid sites that increases with the introduction of copper species. This

could be attributed to the contribution of copper oxide species. Similarly, a heterogeneous

distribution of acid sites for the γ-Al$_2$O$_3$ system is highlighted. A minor or negligible total

amount of acid sites in the SiO$_2$ support was found.
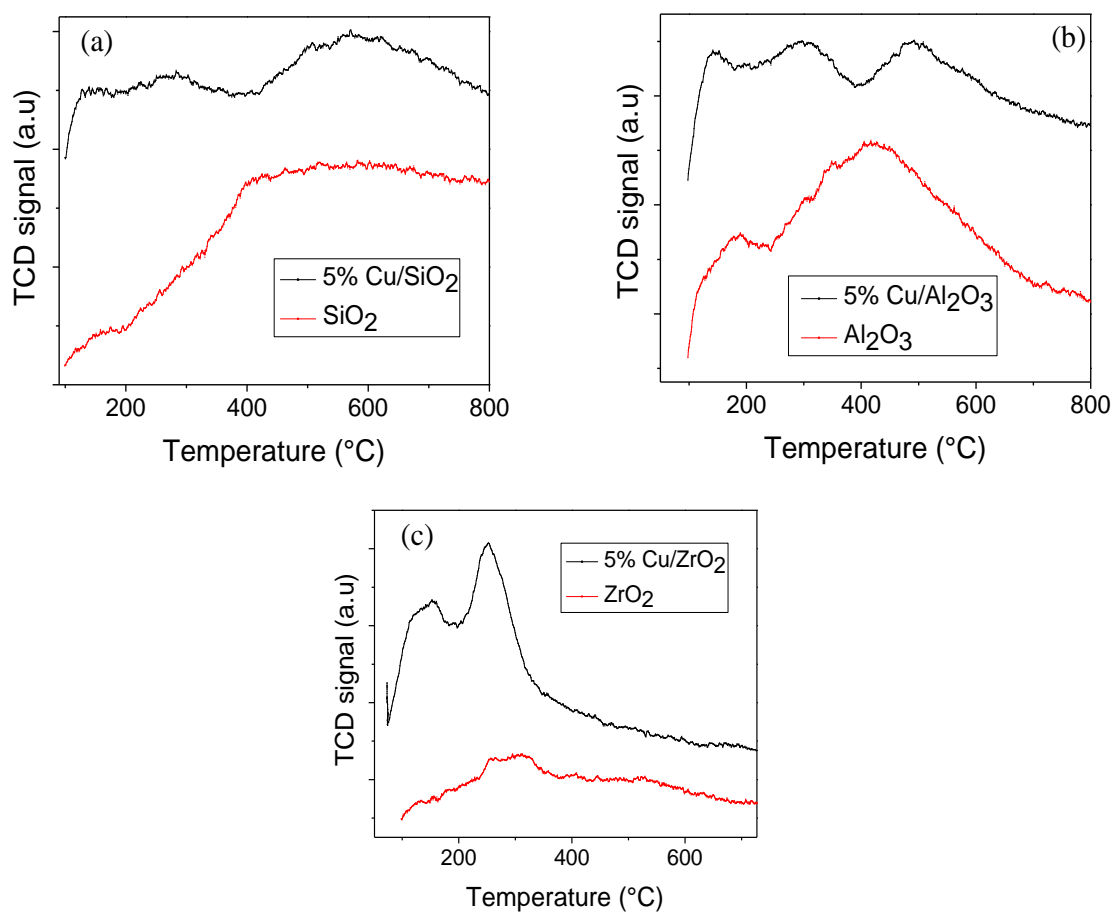
351

352   Fig. 3. Temperature-programmed desorption of ammonia profiles of supports and Cu-based

353   catalysts (a) SiO$_2$ and 5%Cu/SiO$_2$, (b) Al$_2$O$_3$ and 5%Cu/Al$_2$O$_3$ and (c) ZrO$_2$ and 5%Cu/ZrO$_2$.

354

355   Brönsted and Lewis acidity were identified by FTIR of pyridine as shown Fig. 4. The IR

356   spectra of the support materials and supported copper catalysts were compared in the region

357   of 1600-1400 cm^{-1}. From the IR spectra only Lewis acid sites were identified over the support

358   materials. The IR spectra of the supports (γ-Al$_2$O$_3$ and ZrO$_2$) show bands at about 1455, 1490

359   and 1610 cm^{-1} after pyridine desorption at 400 °C. The band observed at 1455 cm^{-1} is attributed

360   to the presence of hydrogen-bonded pyridine adsorbed on Lewis acid sites [53]. The observed

361   band at 1610 cm^{-1} is ascribed to pyridine strongly bound on Lewis acid sites [54]. The band

362   observed at about 1490 cm^{-1} is attributed to pyridine adsorbed on both Lewis and Brönsted

363   acid sites. There is no evidence for a band at about 1610 cm^{-1} (Fig. 4) in the infrared spectra

364   of pyridine desorption on SiO$_2$. In addition, there is no evidence for a band at 1540 cm^{-1}

365   suggesting no Brönsted acidity for SiO$_2$ sample in agreement with literature [55]. It must be

366   added that the absence of the band at 1490 cm^{-1} suggests negligible Lewis acidity in SiO$_2$

367   support.

368

369   Supported copper catalysts were reduced at 400 °C in hydrogen prior the pyridine

370   measurements. Impregnation of copper on ZrO$_2$, γ-Al$_2$O$_3$ and SiO$_2$ resulted in the appearance

371   of Lewis and Brönsted acid sites. The bands corresponding to Brönsted acid sites were

372   observed at 1548 cm^{-1} for copper supported on γ-Al$_2$O$_3$ and ZrO$_2$ [56]. In contrast, Cu/SiO$_2$

373   catalyst exhibited only Lewis acid sites.

374
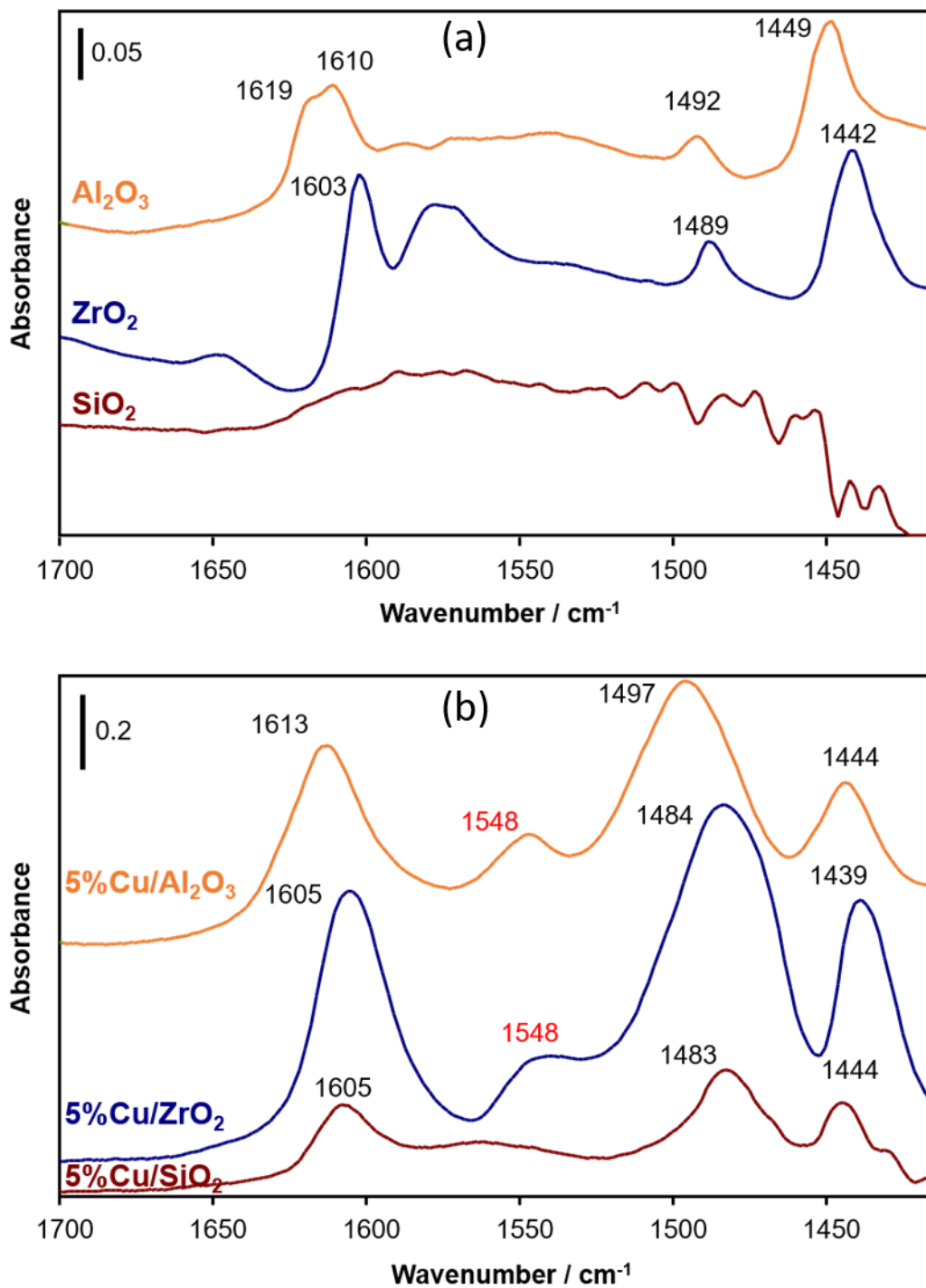
Fig. 4. FTIR of (a) supports and (b) catalyst after pyridine desorption at 400 °C.

375

376

377   TPR profiles of the calcined copper catalysts at 400 °C are shown in Fig. 5. Cu/SiO_2 catalyst

378   exhibits a nearly symmetrical reduction peak at ca. 200 °C. For Cu/Al_2O_3 catalyst, the main

379   reduction peak is also centred at ca. 200 °C. It is observed that the catalysts Cu/SiO_2 and

380   Cu/Al_2O_3 have an reductive event at the same temperature which suggests a homogeneous

381   copper species distribution and the corresponding reduction refers to $Cu^{+2} \rightarrow Cu^0$ [57].

382

383
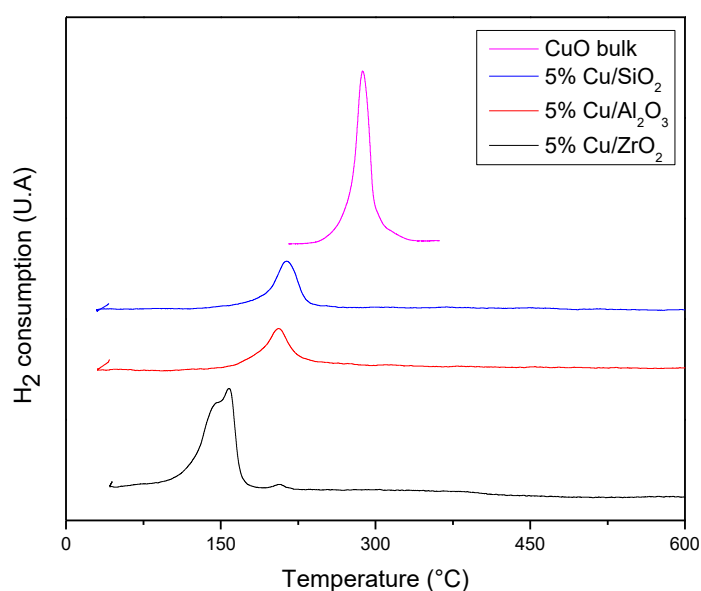
Fig. 5. TPR of copper based catalysts.

394   For Cu/ZrO_2 sample the main reduction peak shifts to lower temperature at ca. 160°C and

395   presents a shoulder peak at ca. 140°C. Liu *et al.* [58] observed two overlapping peaks with

396   apparent maxima at 140°C and 160°C for the reduction of copper supported on tetragonal

397   zirconia. According to these authors, these peaks correspond to highly disperse Cu^{+2} species

398   assigning the first peak to the reduction of $Cu^{+2} \rightarrow Cu^{+1}$, followed by a second event to Cu^{+1}

399    $\rightarrow Cu°$. The reduction profile of Cu/ZrO_2 sample suggests a strong influence of the support

400   on the reduction of copper species. A shift towards lower temperatures with respect to the

401   other two supports (γ-Al$_2$O$_3$ and SiO$_2$) is observed. This is attributed to promoter effects of

402   ZrO$_2$ in the reducibility of copper species. It must be added that only a minor reduction peak

403   at 200^{0}C was visible for Cu/ZrO$_2$. This peak can be attributed to the reduction of bulk CuO

404   [59]. The low reduction temperature strongly suggests the presence of finely dispersed copper

405   species embedded homogeneously in the ZrO$_2$ support. The higher reduction temperature

406   peak is assigned to the reduction of CuO crystallites [60].

407

408   The existence of vacancies on the surface of the support is a vital factor in achieving

409   dispersion of ionic species [61]. Cu^{+2} species can be located at surface vacancies of ZrO$_2$

410   leading to a high dispersion of copper. These species are responsible for the low temperature

411   reduction peaks. Previous work reports a dispersion capacity of 8.6 ions of Cu^{+2} per nm^2 of

412   ZrO$_2$. Loads of copper species higher than this dispersion capacity of ZrO$_2$ will result in the

413   formation of Cu^{+2} ions being gradually surrounded by other Cu^{+2} ions forming CuO bulk

414   species leading to an increase of the reduction temperature of these species [58]. Bulk CuO

415   exhibits a broad TPR peak at ca. 300°C (Fig. 5).

416

417   γ-Al$_2$O$_3$ is also able to stabilize Cu^{+2} due to the existence of tetrahedral and octahedral

418   vacancies on its surface [62], while SiO$_2$ is not able due to its structurally saturated surface.

419   Previous work [63] reported the formation of bulk CuO modulated in terms of the ratio

420   Cu/SSA or "copper charge/specific support area (SSA)" of 4.5 atoms of Cu per nm^2 of ZrO$_2$

421   support. Considering that the ZrO$_2$ used in our work has a specific surface area of 146 m^2 g$^-$

422   ^{1} the appearance of bulk CuO would occur approximately in copper charges of 7 wt.%. In

423 addition, considering that the γ-Al_2O_3 used in our work has a specific surface area of 212 m^2

424 g^{-1} it can be expected that the formation of CuO species would begin to appear with copper

425 loading close to 10 wt.%. The detection of CuO bulk species in the XRD profiles (Fig. 2) is

426 somewhat difficult.

427

428 Dispersion on metallic copper and the specific copper surfaces of the catalysts were

429 determined by chemisorption of N_2O. Cu/ZrO_2 shows the highest dispersion with 38% and

430 the largest metallic surface area of Cu° (Table 4). Although ZrO_2 has the smallest specific

431 surface it is able to disperse substantial amount of impregnated copper species due to the

432 strong interaction between copper species and support [64]. Cu/SiO_2 shows a significantly

433 lower copper dispersion and specific copper surface of the catalysts which are more likely

434 due to a more intense sintering of copper particles.

435

436 Table 4. Catalysts characterization by N_2O chemisorption

Catalyst / Parameter	5%Cu/SiO_2	5%Cu/γ-Al_2O_3	5%Cu/ZrO_2
N_2O (μmol N_2O g_{cat}^{-1})	203	277	301
Dispersion (%)	26	35	38

437

438 XPS parameters from the reduced copper catalysts are summarized in Table 5 and Fig. 6.
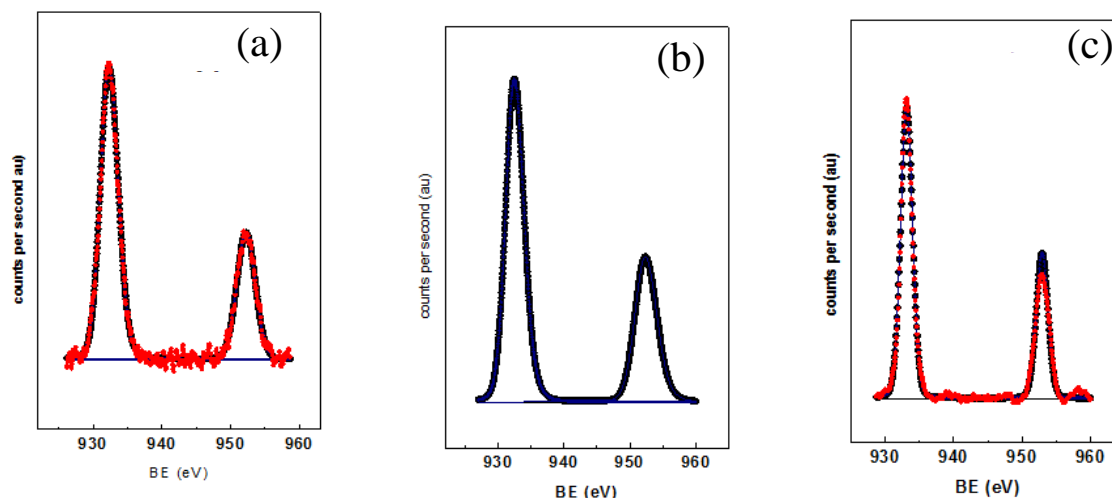
Fig. 6. XPS of (a) 5%Cu/SiO$_2$, (b) 5%Cu/Al$_2$O$_3$ and (c) 5%Cu/ZrO$_2$.

All reduced catalysts exhibited symmetrical Cu3p$_{3/2}$ and Cu2p$_{1/2}$ peaks with binding energies between 932.5 and 952.4 eV respectively. A satellite was not detected at approximately 942 eV suggesting absence of Cu^{+2} species [65]. Because the binding energies of Cu° and Cu$^+$ are similar it is difficult to differentiate them based only on Cu3p$_{3/2}$, so we used the modified Auger parameter (αCu) for further conclusions.

Table 5. Binding energies (eV) of internal levels, Auger parameter and atomic ratios of supported copper catalysts

Catalyst	Cu2p$_{3/2}$	M2p or M3d	αCu (Auger)	Cu/M[a] atomic ratio
5%Cu/ZrO$_2$	932.5	182.2	1850.9	0.016
5%Cu/Al$_2$O$_3$	932.5	74.5	1851.0	0.021
5%Cu/SiO$_2$	932.4	103.4	1850.8	0.027

24

450   The value of αCu at approximately 1851.0 eV for reduced copper catalysts suggests that the

451   copper species may prevail on the catalyst surface as Cu°. The value of the atomic surface

452   ratio Cu/M (M=Al, Si, Zr) determined via XPS for the reduced samples increases in the

453   following order: $Cu/ZrO_2 < Cu/\gamma-Al_2O_3 < Cu/SiO_2$. The difference in the distribution of

454   copper species on each support can be tentatively identified with the Cu/M surface atomic

455   ratio value. In this case, a lower Cu/M suggests a more homogeneous distribution of copper

456   species on ZrO_2 support in agreement with the aforementioned results via XRD (Fig. 2), TPR

457   (Fig. 5), chemisorption of N_2O (Table 4).

458

459   *3.2 Catalytic activity*

460   Glycerol conversion profile in the first 120 minutes of reaction was used to determine the

461   kinetic parameters such as the reaction order (*n*) and the apparent kinetic constant (*k*) values

462   expressed in terms of $min^{-1} m_{cat}^{-2}$. The first 120 minutes have been studied in order to ensure

463   the evaluation of the catalytic performance under conditions where the reaction is kinetically

464   controlled and there is a minimization of the influence of possible product-catalyst

465   interaction. Moreover, for the determination of the kinetic constant an isothermal process;

466   constant volume of the reaction medium and absence of mass transfer effect have been

467   considered. The Weisz-Prater (WP) criterion was used to verify the absence of intraparticle

468   diffusion limitation as well as the assumption of spherical particles and the consideration of

469   an apparent first order reaction. It was obtained a value of WP of 0.12 in the worst scenario.

470   WP values less than 0.3 ensure that there is no mass transfer, thus our system meets the WP

471   criteria. After 2 hours of reaction the conversion observed for $5\%Cu/ZrO_2$, $5\%Cu/Al_2O_3$ and

472    $5\%Cu/SiO_2$ catalysts were at about 30%, 25% and 22%, respectively.

473   In the present study the activity results were expressed in terms of conversion (*X*). The same

474   catalytic test was performed multiple times to check the reproducibility. The results are

475   presented in Fig. 7 with the plot of *–ln(1-X)* versus *time* to demonstrate an apparent kinetic

476   of an irreversible first order reaction with a constant density system. A straight line passing

477   through the origin was obtained (Fig. 7) where the corresponding slope is equal to the

478   apparent kinetic constant of each catalyst. It was represented the results from the repeated

479   experiments for each catalyst in the corresponding plot. The highest kinetic constant was

480   found for the 5%Cu/ZrO$_2$ catalyst.

481

482

483
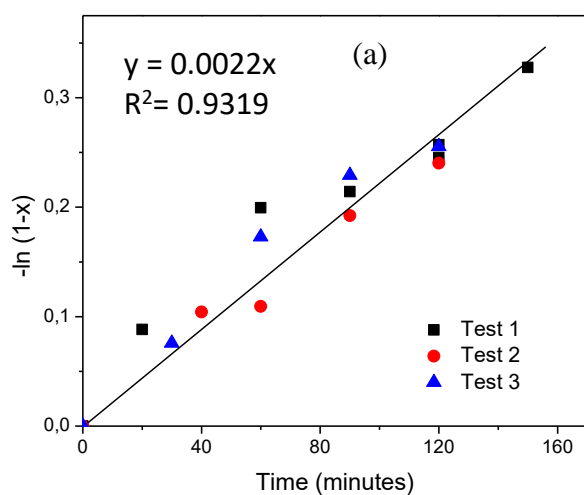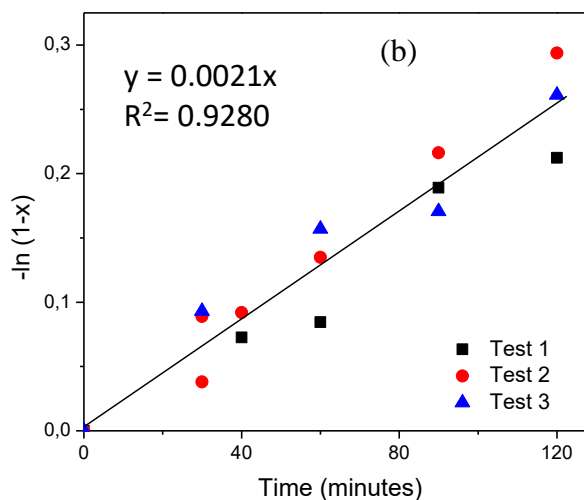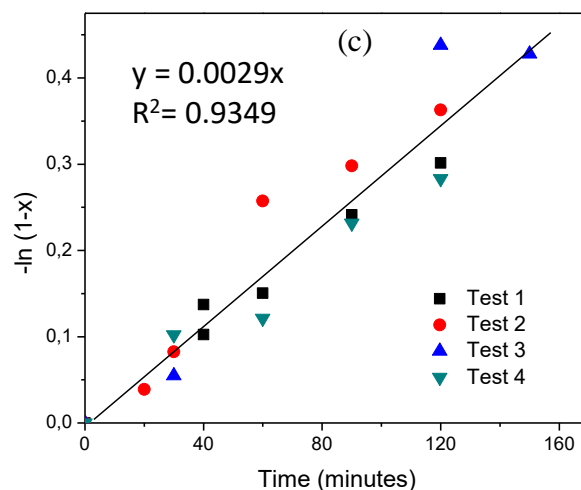
Fig. 7. Reaction demonstrating an apparent first order kinetic (a) 5%Cu/SiO$_2$, (b) 5%Cu/Al$_2$O$_3$ and (c) 5%Cu/ZrO$_2$.

The physical-chemical properties of the support have vital influence on the dispersion of metallic copper species influencing the catalytic performance as noticed in Table 6, which represents the relationship of the kinetic constants expressed in µmol m$_{cat}^{-2}$ with the total quantity of N$_2$O chemisorbed (µmol m$_{cat}^{-2}$). Table 6 also shows the relationship of the corresponding kinetic constants to the total acidic sites expressed in (µmol m$_{cat}^{-2}$). Thus, an increase in the apparent kinetic constant with both total quantity of N$_2$O chemisorbed and the total quantity of acidic sites was observed.

Table 6. Apparent kinetic constant of the copper catalysts

| Apparent first order kinetic constant, k	5%Cu/SiO$_2$	5%Cu/γ-Al$_2$O$_3$	5%Cu/ZrO$_2$
k (min^{-1})	0.0022	0.0021	0.0029
k (min^{-1} m$_{cat}^{-2}$)	4.5×10^{-6}	5.8×10^{-6}	1.1×10^{-5}

498   Under the experimental conditions, a negligible conversion of glycerol and hydroxyacetone

499   selectivity were observed when the supports were directly used as catalysts in the activity

500   tests. Fig. 8 shows their catalytic performance monitored in different times of reaction.

501   Cu/ZrO$_2$ catalyst (Fig. 8a) shows a glycerol conversion of at about 4% at 20 minutes reaching

502   at about 30% of conversion at 120 minutes of reaction. Cu/γ-Al$_2$O$_3$ (Fig. 8b) exhibits a

503   glycerol conversion between 8 to 25% in the range of 120 minutes of reaction. In the case of

504   Cu/SiO$_2$ catalyst (Fig. 8c) it is observed a glycerol conversion of 8% at 20 minutes of reaction

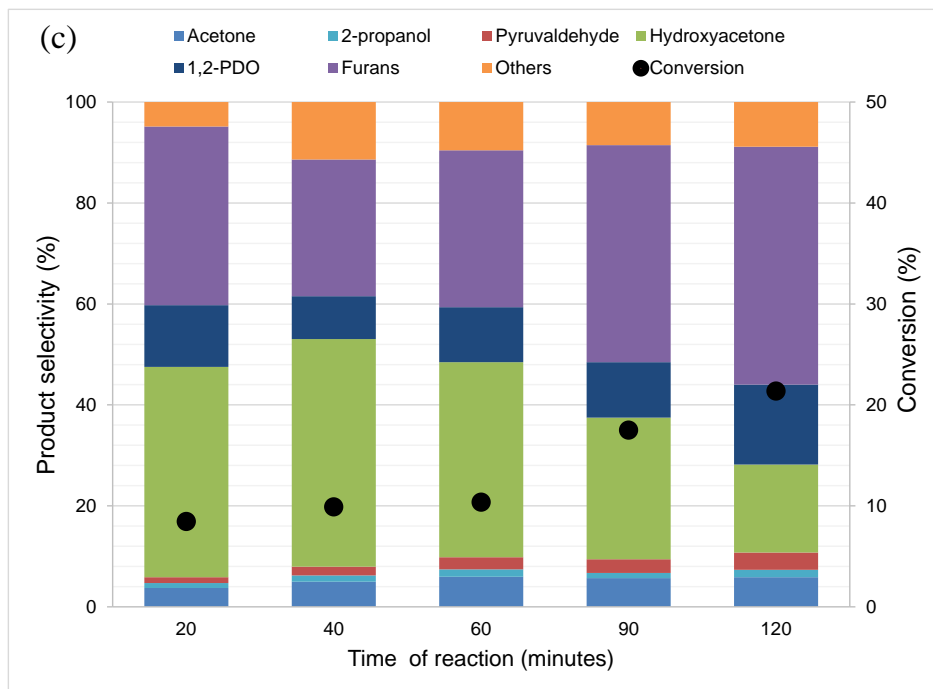505   and at about 20% of conversion at 120 minutes of reaction.

506

507

508
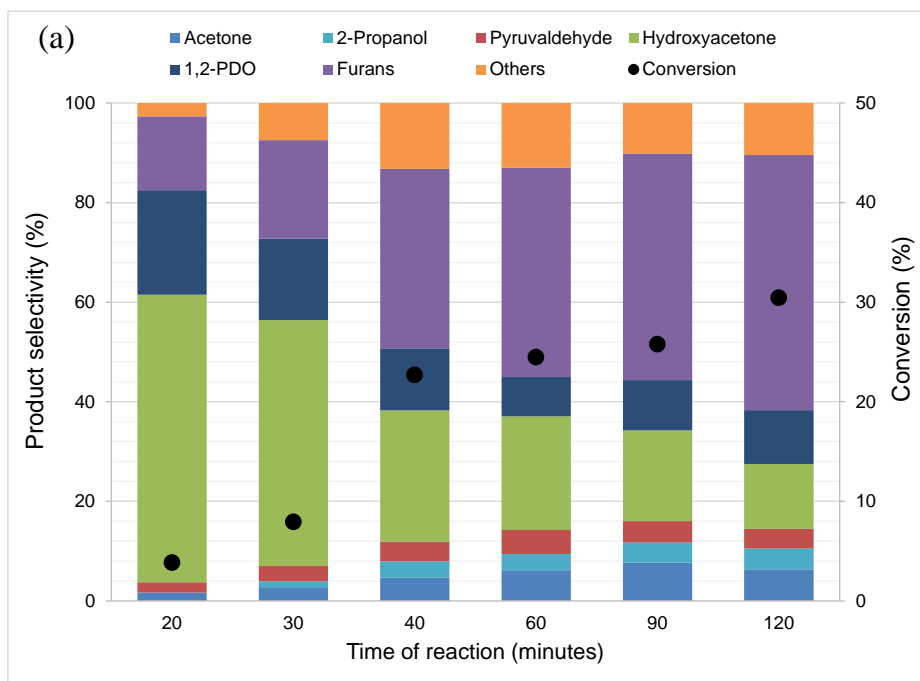
509
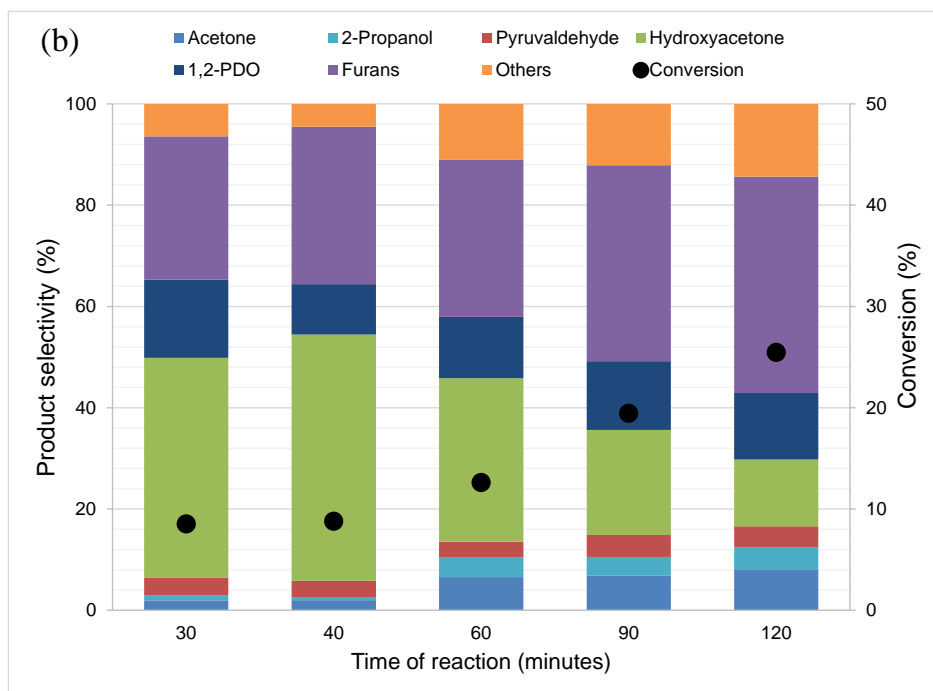
510

511

512 Figure 8. Catalytic performance of copper based catalysts. (a) 5%Cu/ZrO$_2$, (b) 5%Cu/Al$_2$O$_3$

513 and (c) 5%Cu/SiO$_2$.

514

515   The main products observed in the reaction was acetone, 2-propanol, pyruvaldehyde,

516   hydroxyacetone, 1,2-propanediol, furan derivatives and other unidentified compounds

517   possibly produced by secondary reactions between the compounds in the reaction mixture. It

518   is noticed for the copper catalysts that the highest selectivity towards hydroxyacetone was in

519   first minutes of reaction. In this respect, hydroxyacetone selectivity of 57% and 41% was

520   observed respectively for Cu/ZrO_2 and Cu/SiO_2 catalysts at 20 minutes of reaction, whereas

521   for $Cu/\gamma\text{-}Al_2O_3$ sample a hydroxyacetone selectivity of 43% was noticed at 30 minutes of

522   reaction. Previous work [9] reported over Cu-Al (50:50) catalyst prepared by coprecipitation

523   a hydroxyacetone selectivity of 92% and 24% of glycerol conversion at 493 K in aqueous

524   medium under N_2 atmosphere in autogenous condition. W. Suprun *et al.* [66] reported

525   hydroxyacetone selectivity of 23% and 100% of conversion in the dehydration of glycerol

526   over $Al_2O_3\text{-}PO_4$ catalyst at 280^0C. Chiu et al.[16] reported that copper-chromite catalyzes the

527   dehydration of glycerol with a selectivity towards hydroxyacetone of 70% and 22% of

528   glycerol conversion.

529

530   Hydroxyacetone was the major product observed in the initial reaction period as shown Fig.

531   9. In addition, the highest yield towards hydroxyacetone was noticed for $5\%Cu/ZrO_2$.

532   Hydroxyl terminal groups of the glycerol molecule interacting with the Lewis acid sites on

533   the catalyst surface may promote the formation of an enol intermediate which rapidly

534   reorganizes to form hydroxyacetone. Thus, hydroxyacetone can be obtained by direct

535   dehydration of glycerol followed by a keto-enolic tautomerization [67]. Pyruvaldehyde was

536   also observed and it can be formed from hydroxyacetone dehydrogenation.

537
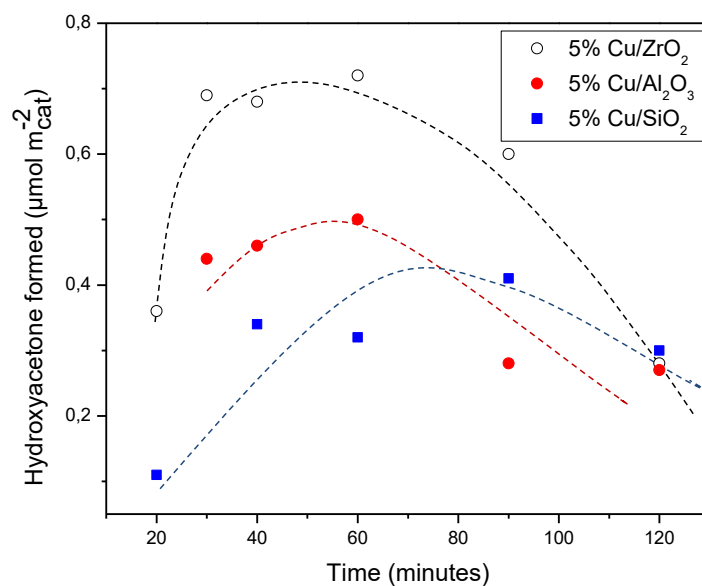
Fig. 9. Glycerol conversion towards hydroxyacetone. (Dashed lines only serve to guide the

eyes).

After 120 minutes of reaction, acetone, 2-propanol and furan derivatives were also observed.

These products were formed from the degradation of hydroxyacetone. Earlier works report

that hydroxyacetone is converted to carboxylic acids which allow acetone to be formed via

ketonization. Catalytic cyclisation to form furan derivatives are also observed. It must be

added that 1,2 propanediol (1,2-PDO) was also detected. Previous work [9] reported that

glycerol hydrogenolysis to 1,2-PDO proceeds through a dehydrogenation-dehydration-

hydrogenation mechanism. In that case hydroxyacetone is the intermediate to 1,2-PDO.

Copper may serve as active sites for the subsequent hydrogenation step to 1,2-PDO by the

formation of active hydrogen atom originating from the dehydrogenation step. The general

chemical route based on the main products detected by gas chromatograph and mass

spectrometry is shown in Scheme 1.

Furan derivatives

Acetone

Glycerol   Hydroxyacetone   1,2-PDO   2- Propanol

Pyruvaldehyde
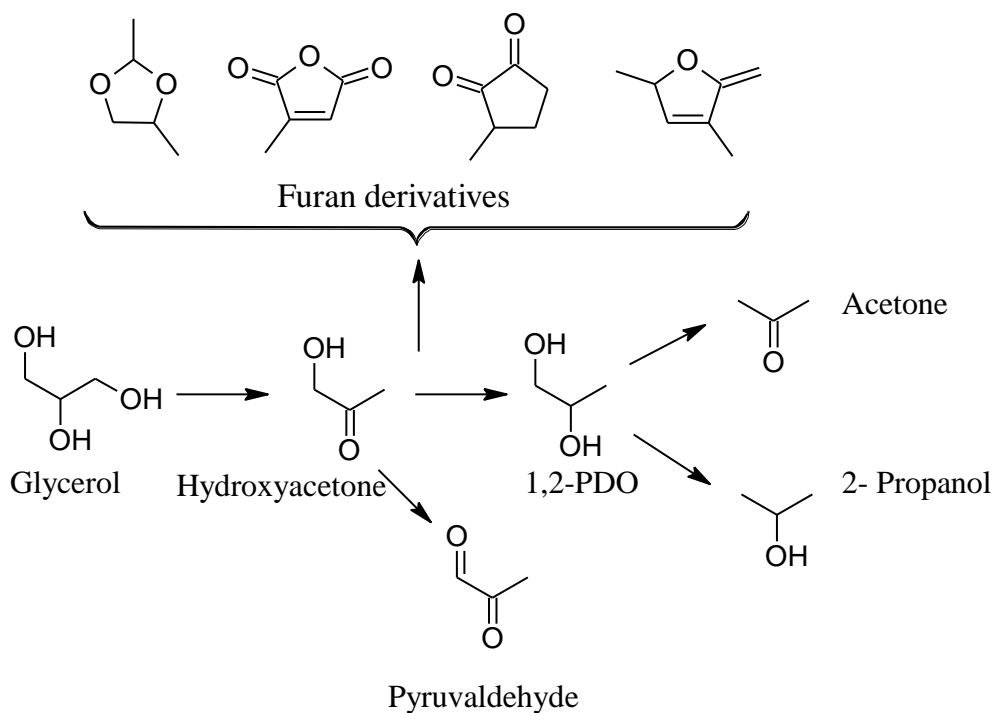
553

554   Scheme 1. Identified products in the glycerol dehydration.

555

556   *3.3 Catalyst Recycling*

557   The recycling of 5%Cu/ZrO$_2$ catalyst during the selective conversion of glycerol to

558   hydroxyacetone was investigated. After the first test (Postcycle 1), the catalyst was recovered

559   by decantation and it was washed with a 50/50 mixture methanol-water and dried at 100°C.

560   The dried catalysts were calcined at 400 °C for 4 hours and finally reduced at 400 °C for 4

561   hours under hydrogen flow. The resultant reduced catalyst was used for the next cycle

562   (Postcycle 2) under conditions that allowed to maintain the same glycerol/catalyst molar ratio

563   used in the cycle 1. The same process of separation, washing and reactivation of the catalyst

564   has been implemented for the Postcycle 3. As shown Fig. 10 the fresh 5%Cu/ZrO$_2$ gives at

565   about 30% of glycerol conversion at 120 minutes of reaction. During the Postcycle 2 the

conversion of glycerol decreased to about 10% and in the third cycle the conversion

decreased to reach at about 5%.
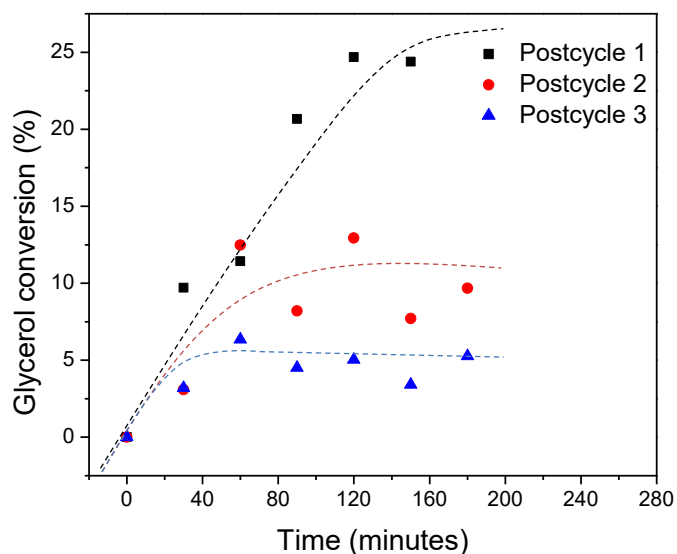
Fig. 10. 5%Cu/ZrO$_2$ catalyst recycling process in the glycerol dehydration. (Dashed lines only serve to guide the eyes).

To identify the origin of the deactivation, the fresh and used 5% Cu/ZrO$_2$ catalysts (reactivated by calcination-reduction) were characterized by nitrogen physisorption (Fig. S1 and Table 7) and N$_2$O chemisorption (Fig. S2 and Table 7). In addition, X-ray diffraction (Fig. S3) and scanning electron microscopy coupled to an energy dispersive X-ray spectrometer (SEM-EDS) (Table 7) were performed. The EDS results indicate that copper species are homogeneously distributed over ZrO$_2$ and there is no appreciable variation in the atomic relationship Cu/Zr after each recycling (Table 7).

583   Table 7. Properties of the 5%Cu/ZrO$_2$ catalyst during the recycling process

Sample	S$_{BET}$ (m^2 g^{-1})	V$_P$ (cm^3 g^{-1})	d$_p$ (nm)	N$_2$O (µmol N$_2$O g$_{cat}^{-1}$)	Cu/Zr[a]
Fresh	131	0.13	4.01	301	0.075
Postcycle 1	128	0.15	4.24	286	0.090
Postcycle 2	129	0.15	4.55	164	0.075
Postcycle 3	116	0.14	4.86	170	0.079

584   [a] EDS

585

586   Change of the textural properties of 5%Cu/ZrO$_2$ material in the recycling was negligible

587   (Table 7). The total amount of chemisorbed N$_2$O was progressively reduced between each

588   cycle (Fig. S2 and Table 7). Moreover, the X-ray diffraction of the used materials after each

589   reactivation indicates some sintering of copper species by the appearance of copper oxide

590   phase (Fig. S3). The observed sintering of copper particles after the catalytic cycles may

591   result in the loss of active site which can be considered as the main factor contributing to the

592   observed catalyst deactivation.

593

594   *3.4 DFT study*

595

596   To gain molecular insights and explain the support effects, adsorption energies of glycerol,

597   and hydroxyacetone were computed using DFT calculations. The effect of hydroxylation on

598   Al$_2$O$_3$ and ZrO$_2$ supports due to water dissociation, which is also related to Brönsted acid site

599   were also investigated. Three possible adsorption sites were considered on each surface i.e.

600   Cu site, Al or Zr site on support and interface site between Cu cluster and support. Here, we

601 report only adsorption at the most stable one. The adsorption energies were calculated using

602 equation (9) and summarized in Table 8.

603 $$E_{ad} = E_{total} - E_{clean\ surface} - E_{adsorbate} \qquad (9)$$

604

605 where E_{ad} is adsorption energy, E_{total} is energy of structures with glycerol/hydroxyacetone

606 adsorption, $E_{clean\ surface}$ is energy of structures without glycerol/hydroxyacetone

607 adsorption and $E_{adsorbate}$ is energy of isolated glycerol/hydroxyacetone molecule. The more

608 negative values of E_{ad}, the stronger adsorption.

609

610 Table 8. Adsorption energies (kJ mol^{-1}) of glycerol and hydroxyacetone on Cu(111),

611 Cu_{13}/Al_2O_3(110), Cu_{13}/ZrO_2(111), Cu_{13}/hydroxylated Al_2O_3(110), and Cu_{13}/hydroxylated

612 ZrO_2(111) surfaces and Bader charge analysis of Cu_{13} cluster. The corresponding adsorption

613 structures are shown in Fig. 11.

614

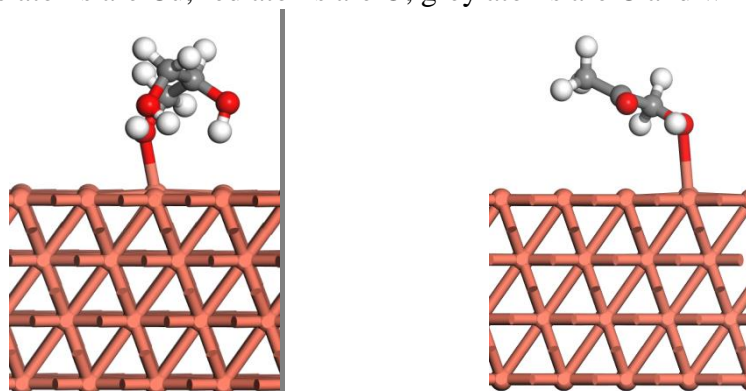615

|	Adsorption energy (kJ mol^{-1})		Charge of Cu_{13} cluster (e$^-$)
	glycerol	hydroxyacetone	
Cu(111)	-100.12	-102.13	
Cu_{13}/Al_2O_3(110)	-337.77	-252.71	+0.13
Cu_{13}/hydroxylated Al_2O_3(110)	-337.86	-274.01	+0.55
Cu_{13}/ZrO_2(111)	-151.04	-178.36	-0.28
Cu_{13}/hydroxylated ZrO_2(111)	-127.78	-159.66	-0.51

616
617

618 (a) Cu(111)

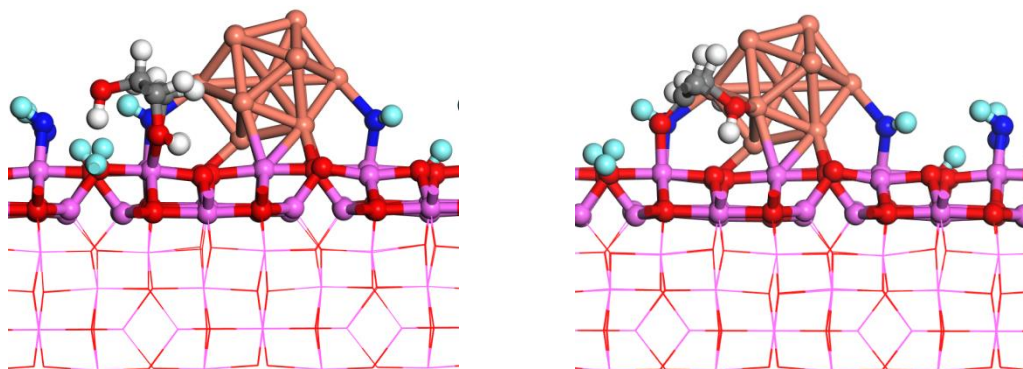619 Orange atoms are Cu, red atoms are O, grey atoms are C and white atoms are H.

620

621

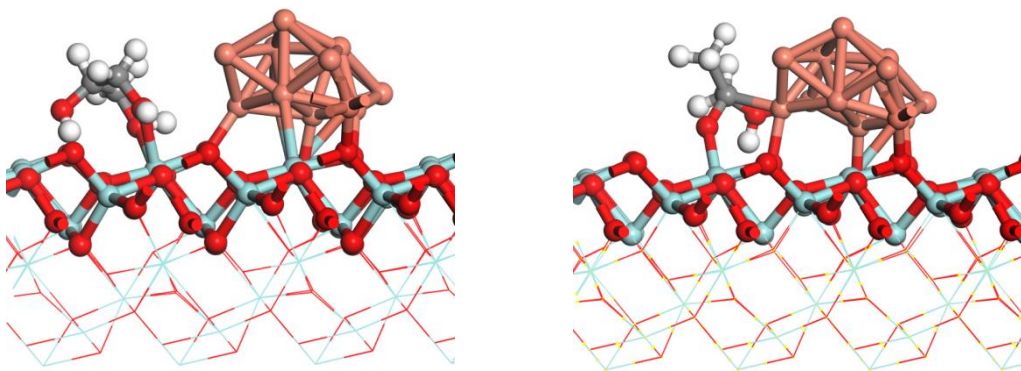622 (b) Cu$_{13}$/Al$_2$O$_3$(110)

623 Purple atoms are Al.
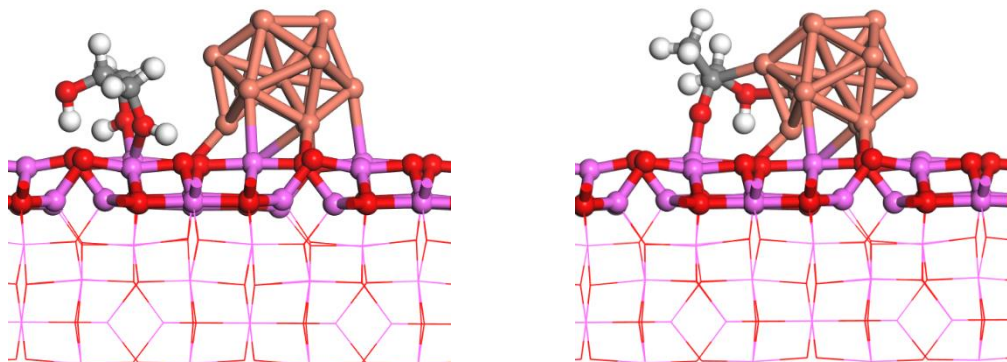
624

625

626 (c) Cu$_{13}$/hydroxylated Al$_2$O$_3$(110)

627 Blue atoms and light green atoms are O and H from hydroxylation, respectively.

628

629

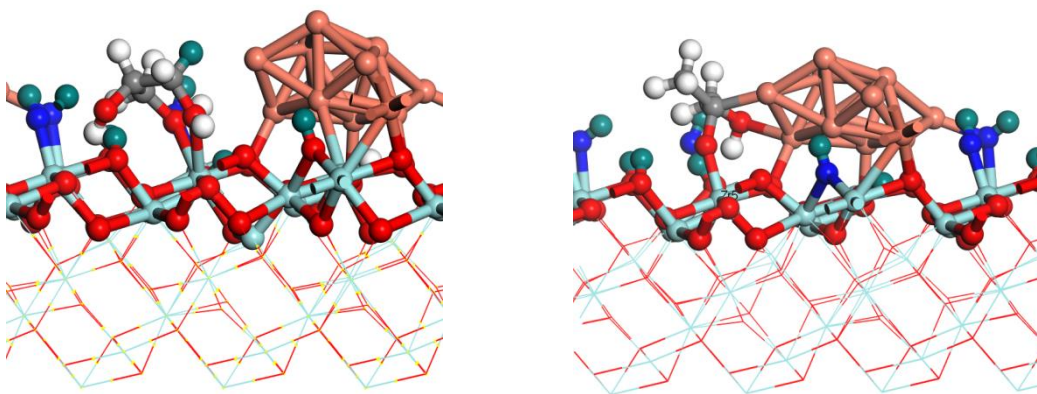630 (d) Cu$_{13}$/ZrO$_2$(111)

631 Light green atoms are Zr.

632

633

634   (e) Cu$_{13}$/ hydroxylated ZrO$_2$(111)
635   Blue atoms and dark green atoms are O and H from hydroxylation, respectively.

636

637

638   Fig. 11. Most stable adsorption structures of glycerol (left) and hydroxyacetone (right) on (a)

639   Cu(111), (b) Cu$_{13}$/Al$_2$O$_3$(110), (c) Cu$_{13}$/hydroxylated Al$_2$O$_3$(110), (d) Cu$_{13}$/ZrO$_2$(111), and

640   (e) Cu$_{13}$/hydroxylated ZrO$_2$(111) surfaces.

641

642   Glycerol and hydroxyacetone adsorption strength are in the order of Cu(111) <

643   Cu$_{13}$/ZrO$_2$(111) < Cu$_{13}$/Al$_2$O$_3$(110). The relatively strong adsorption indicates that the

644   support significantly facilitate interaction with glycerol and hydroxyacetone. The strong

645   glycerol adsorption on Cu$_{13}$/Al$_2$O$_3$(110) and Cu$_{13}$/ZrO$_2$(111) surfaces could result from

646   bidentate binding that both oxygen ends of glycerol molecule bond to the same metal atom

647   of support (Al or Zr) whereas monodentate binding occurs on Cu(111) surface (Fig. 11, left).

648   Hydroxyacetone prefers to bind through oxygen atom of hydroxyl group on Cu(111) surface

649   while it binds at the interface site where oxygen of carbonyl group interacts with metal site

650   of support and oxygen of hydroxyl group interacts with copper site (Fig. 11, right). Thus,

651   hydroxyacetone interaction on $Cu_{13}/Al_2O_3(110)$ and $Cu_{13}/ZrO_2(111)$ surfaces is significantly

652   stronger than that on Cu(111) surface. As illustrated in Fig. 11, glycerol favours to adsorb at

653   support's metal atom site locating adjacent to the Cu cluster and hydroxyacetone prefers to

654   adsorb at the interface site requiring both support's metal atom site and Cu site. This suggests

655   the vital synergistic role of the interface Cu-support as the active site and the significance of

656   high copper particles dispersion, in which turn the increase of interfacial Cu-support sites.

657   Hydroxylation on $Cu_{13}/Al_2O_3(110)$ and $Cu_{13}/ZrO_2(111)$ surfaces induce different impact on

658   binding strength. Hydroxylation on $Cu_{13}/Al_2O_3(110)$ facilitates hydroxyacetone adsorption

659   to be stronger while it weakens glycerol and hydroxyacetone adsorption on $Cu_{13}/ZrO_2(111)$,

660   yet the favourable adsorption site and adsorption characteristic (monodentate/bidentate) are

661   similar to those without hydroxylation.

662   Furthermore, Bader charge analysis (Table 8) of Cu_{13} cluster was performed to better

663   understand the effect of support. Cu_{13} supported on Al_2O_3 lose electrons to Al_2O_3 showing

664   positive charge while Cu_{13} supported on ZrO_2 gain electrons from ZrO_2 showing negative

665   charge. It is implied that ZrO_2 support shows stronger acidity compared to Al_2O_3 support.

666   The hydroxylation increases the degree of electrons transfer from Cu_{13} cluster to Al_2O_3 and

667   from ZrO_2 to Cu_{13} cluster resulting in higher positive charges of supported Cu_{13} on Al_2O_3

668   and higher negative charge of supported Cu_{13} on ZrO_2.

669

670   **4. Discussion**

671 To establish relationships between activity and structural parameters the copper based

672 catalysts were evaluated in the glycerol dehydration. Fig. 12 illustrates a plot correlating the

673 produced hydroxyacetone expressed in terms of $\mu mol\ m_{cat}^{-2}$ at 20% of conversion with the

674 total number of exposed metallic copper species expressed in terms of the total quantity of

675 chemisorbed N_2O (Y_{N2O}, $\mu mol\ N_2O\ m_{cat}^{-2}$) and with the total number of acid sites of the

676 catalysts expressed in terms of $\mu mol\ NH_3\ m_{cat}^{-2}$.

677
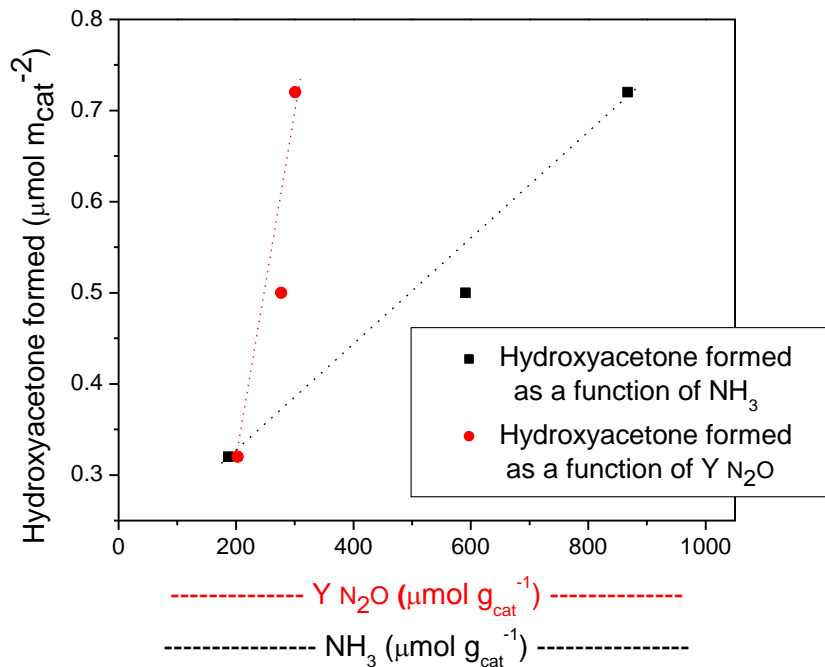
678

679 Fig. 12. Relationship between the total quantity of the produced hydroxyacetone versus

680 exposed metallic copper atoms and the total quantity of acidic sites. (Dashed lines only serve

681 to guide the eyes).

682

683 In the formation of hydroxyacetone stands out a lower sensitivity to the total number of acidic

684 sites compared to the total number of exposed copper atoms which is reflected in the quantity

685 of chemisorbed N_2O. A lower quantity of chemisorbed N_2O exhibits a higher hydroxyacetone

686 yield when compared with the same quantity of acidic sites (μmol NH_3 m_{cat}^{-2}).

687

688 The calculation results also reveal that hydroxyacetone and glycerol bind stronger on

689 $Cu_{13}/Al_2O_3(110)$, $Cu_{13}/ZrO_2(111)$ surfaces compared to $Cu(111)$ surface. Also, glycerol is

690 favourable to adsorb at support metal site close to copper cluster and hydroxyacetone is

691 favourable to adsorb at the interface copper-support site (Fig. 11 (right)). These results

692 suggest the synergistic role of acid sites (Al or Zr) of supports and copper cluster to promote

693 hydroxyacetone and glycerol interaction with surfaces. In addition, the active role of the

694 interfacial sites suggests the positive effects of highly dispersed Cu over support on catalytic

695 reactivity. The DFT calculations also indicate that stronger acidity of ZrO_2 may better

696 promote moderate interaction with intermediates while relatively weak acidity of Al_2O_3

697 results in too strong interaction with intermediates. Furthermore, the negative charges of

698 supported Cu cluster on ZrO_2 may indicate the number of acid sites increase with copper

699 introduction on ZrO_2 support.

700

701 It should be added that the highest kinetic constant indicates that the most active catalyst is

702 the 5%Cu/ZrO_2 catalyst. Particularly, ZrO_2 has been described as a preventive element for

703 sintering copper species and it is therefore considered to be a structural promoter [68]. It is

704 important to complement that the results of TPR indicate that the presence of ZrO_2 facilitates

705 the reduction of copper species, as well as the results of XRD, N_2O chemisorption, EDS and

40

706 XPS which suggest that ZrO_2 support leads to a homogeneous distribution of copper species

707 and higher dispersion of the copper species compared with γ-Al_2O_3 and SiO_2. In addition,

708 pyridine infrared indicates that 5%Cu/ZrO_2 and 5%Cu/γ-Al_2O_3 catalysts present both acidic

709 sites of Lewis and Brönsted. For 5%Cu/SiO_2 only Lewis acid sites were found.

710

711 5. Conclusions

712

713 The dehydration reaction of glycerol to hydroxyacetone on copper based catalysts suggests

714 apparent first order kinetics. By NH_3-TPD, it has been observed that the 5%Cu/ZrO_2

715 exhibited the highest total quantity of acidic sites and total amount of N_2O chemisorbed

716 suggesting higher dispersion of copper species compared with 5%Cu/γ-Al_2O_3 and

717 5%Cu/SiO_2 catalysts. XRD analysis suggests that copper species are finely dispersed on the

718 support. XPS analysis identified that copper species are found in metallic state at the catalyst

719 surface and the atomic ratio (Cu/M) (M= Si, Al or Zr) suggests that copper species are more

720 homogeneously distributed on ZrO_2 surface.

721

722 Complementary study of DFT indicates that both glycerol and hydroxyacetone adsorb

723 significantly stronger on Cu_{13}/γ-Al_2O_3 (110) and Cu_{13}/ZrO_2 (111) compared to Cu (111)

724 which further suggests that the active sites for glycerol and hydroxyacetone adsorption are

725 the metal support site and the dual site consisting of Al or Zr of the support (ZrO_2 and γ-

726 Al_2O_3) of the copper species.

727

41

728   The kinetic constants expressed in μmol m_{cat}^{-2} indicate that the most active material for

729   glycerol dehydration has been the 5%Cu/ZrO$_2$ catalyst. A linear correlation between the yield

730   of hydroxyacetone expressed in terms of μmol m_{cat}^{-2} with the total quantity of chemisorbed

731   N$_2$O and the total quantity of acidic sites suggest that the copper dispersion is a sensitivity

732   factor for the activity in the glycerol dehydration.

733

734   The sintering of copper particles between each catalyst recycling step by the thermal

735   activation process (calcination-reduction) is the main descriptor responsible for the lost in

736   the activity for the 5%Cu/ZrO$_2$ in the recycling study in agreement with the progressive

737   decrease in the total quantity of N$_2$O chemisorbed after each cycle. In addition, the

738   characterization by EDS did not indicate appreciable variation in the atomic Cu/Zr ratio

739   between each one of the reactions in the recycling process.

740

745

746   **References**

747   [1] S. Sato, M. Akiyama, R. Takahashi, T. Hara, K. Inui, M. Yokota, Appl. Catal A-Gen. 347

748   (2) (2008) 186-191.

749   [2] A. Corma, S. Iborra, A. Velty, Chem. Rev. 107 (6) (2007) 2411-2502.

750 [3] M. Dasari, P-P. Kiatsimkul, W. Sutterlin, G. Suppes, Appl. Catal. A-Gen., 281 (1-2)

751 (2005) 225-231.

752 [4] J. Shabaker, G. Huber, J. Dumesic, J. Catal., 222 (1) (2004) 180-191.

753 [5] A. Corma, G. Huber, L. Sauvanaud, P. O´Connor, J. Catal. 247 (2), (2007) 307-327.

754 [6] S. Demirel, K. Lehnert, M. Lucas, P. Claus, Appl. Catal. B. 70 (1-4) (2007) 637-643.

755 [7] J. Barrault, Y. Pouilloux, J. Clacens, C. Vanhove, S. Bancquart, Catal. Today 75 (1-4)

756 (2002) 177-181.

757 [8] A. Corma, S. Hamid, S. Iborra, A. Velty, J.Catal. 234 (2) (2005) 340-347.

758 [9] R. Mane, A. Yamaguchi, A. Malawadkar, M. Shirai, C. Rode, RSC Adv. 3 (37) (2013)

759 16499-16508.

760 [10] M. Aresta, A. Dibenedetto, F. Nocito, C. Ferragina, J Catal. 228 (1) (2009) 106-114.

761 [11] G. Yang, Y. Ke, H. Ren, C. Liu, R. Yang, W. Dong, Chem.Eng J. 283 (2016) 759-767.

762 [12] M. Mohamad, R. Awang, W. Zin, Am. J. Appl. Sci. 8 (11) (2001) 1135-1139.

763 [13] R. Disselkamp, B. Harris, T. Hart, Catal. Commun. 9 (13) (2008) 2250-2252.

764 [14] J. Ko, I. Kim, S. Yoo, B. Min, K. Kim, C. Park, J. Bacteriol. 187 (16) (2005) 5782-5789.

765 [15] S. Sato, D. Sakai, F. Sato, Y. Yamada, Chem. Lett. 41(9) (2012) 965–966.

766 [16] C. Chiu, A. Tekeei, W. Sutterlin, J.Ronco, G. Suppes, *AIChE J. 54 (9)* (2008) 2456-

767 2463.

768 [17] A. Alhanash, E. Kozhevnikova, I. Kozhevnikov, Appl. Catal. A-Gen. 378 (1) (2010) 11-

769 18.

770 [18] S. Zhu, X. Gao, Y. Zhu, Y. Zhu , H. Zheng, Y. Li, J. Catal. 303 (2013) 70-79.

771 [19] S. Zhu, X. Gao, Y. Zhu, W. Fan, J. Wang, Y. Li, Catal. Sci. Technol. 5 (2) (2005) 1169-

772 1180.

773   [20] P. Hirunsit, C. Luadthong, K. Faungnawakij, RSC Adv. 15(5) (2015) 1118-11197.

774   [21] A. Bienholz, H. Hofmann, P. Claus, Appl. Catal. A-Gen. 391 (1-2) (2011) 153-157.

775   [22] S. Zhu, X.Gao, Y. Zhu, W. Fan, J. Wang, Y. Li, Catal. Sci. Technol. 5 (2) (2005) 1169-

776   1180.

777   [23] H. S. Fogler, Elements of Chemical Reaction Engineering, 3rd edition, Prentice Hall

778   International Series, 1988.

779   [24] O. Levenspiel, Chemical Reaction Engineering, 2nd edition, Wiley International edition,

780   1980.

781   [25] M. Digne, P. Sautet, P. Raybaud, P. Euzen, H. Toulhoat, J. Catal. 226 (2004) 54-68.

782   [26] P. Nortier, P. Fourre, A. B. M. Saad, O. Saur, J.C. Lavalley, Applied Catalysis 61 (1990)

783   141-160.

784   [27] X. Krokidis, P. Raybaud, A. E. Gobichon, B. Rebours, P. Euzen, H. Toulhoat, The

785   Journal of Physical Chemistry B 105(22) (2001) 5121-5130.

786   [28] J. P. Chou, H. Y. T. Chen, C. R. Hsing, C. M. Chang, C. Cheng, and C. M. Wei, Phys.

787   Rev. B 80 (2009) 165412.

788   [29] M. J. Piotrowski, P. Piquini, J. L. F. da Silva, Phys. Rev. B 81 (2010) 155446.

789   [30] T. T. Li, C. He, W.X. Zhang, M. Cheng, Applied Surface Science 479 (2019) 39-46.

790   [31] W. Zeng, J. Tang, P. Wang, Y. Pei, RSC Advances 6(61) (2016) 55867-55877.

791   [32] S. Chen, X. Chen, H. Zhang, Journal of Materials Science **52**(6) (2017) 3162-3168.

792   [33] H. Gao, RSC Advances, 2016. 6(105): p. 102914-102923.

793   [34] P. Hirunsit, K.-ichi Shimizu, R. Fukuda, S. Namuangruk, Y. Morikawa, M. Ehara, The

794   Journal of Physical Chemistry C 118(15) (2014) 7996-8006.

795   [35] C. H. Hu, C. Chizallet, C. M. Maury, M. C. Valero, P. Sautet, H. Toulhoat, P. Raybaud,

796   Journal of Catalysis 274 (1) (2010) 99-110.

797   [36] C. Dessal, A. Sangnier, C. Chizallet, C. Dujardin, F. Morfin, J. L. Rousset, M. Aouine,

798   M. Bugnet, P. Afanasiev, L. Piccolo, Nanoscale 11 (2019) 6897-6904.

799   [37] P. Lackner, J. Hulva, E. M. Köck, W. M. Schmölzer, J. J. Choi, S. Penner, U. Diebold,

800   F. Mittedonfer, J. Redinger, B. Klötzer, G. S. Parkinson, M. Schmid, J. Mater. Chem. A 6

801   (2018) 17587-17601.

802   [38] G. Kresse, J. Furthmüller, Computational Materials Science **6**(1) (1996) 15-50.

803   [39] G. Kresse, J. Furthmüller, Physical Review B, **54**(16) (1996) 11169-11186.

804   [40] J.P. Perdew, K. Burke, M. Ernzerhof, Physical Review Letters **77**(18) (1996) 3865-3868.

805   [41] P.E. Blöchl, Physical Review B 50(24) (1994) 17953-17979.

806   [42] G. Kresse, D. Joubert, Physical Review B 59(3) (1999) 1758-1775.

807   [43] S. Grimme, J. Comput. Chem. 2006, 27, 1787-1799.

808   [44] S. Grimme, J. Antony, S. Ehrlich, H. Krieg, J. Chem. Phys. 2010, 132, 154104.

809   [45] C.L. Fu, K.M. Ho, Physical Review B 28(10) (1983) 5480-5486.

810   [46] H.J. Monkhorst, J.D. Pack, Phys. Rev. B, 13(12) (1976) 5188-5192.

811   [47] G. Henkelman, A. Arnaldsson, H. Jonsson, Comput. Mater. Sci. 36 (2006) 354−360.

812   [48] E. Sanville, S. D. Kenny, R. Smith, G. Henkelman, J. Comput. Chem. 2007, 28,

813   899−908.

814   [49] W. Tang, E. Sanville, G. Henkelman, J. Phys.: Condens. Matter 2009, 21, 084204

815   [50] K. Sing, Pure Appl.Chem.,54 (11), 2201-22l8.

816   [51] F. López, A. Bueno, M. Illán, Appl. Catal. B-Environ. 84(3-4) (2008) 651-658.

817 [52] R. Friedman, J. Freeman, F. Lytle, J. Catal. 55 (1) (1978) 10-28.

818 [53] J. Aguado, J.M. Escola, M.C. Castro, B. Paredes, Appl Catal A Gen 284 (2005) 47–57.

819 [54] B. Chakraborty, B. Viswanathan, Catal Today 49 (1999) 253–260.

820 [55] S. E. Voltz, A. E. Hirscheler, A. Smith, J. Phys. Chem. 64 (1960) 1594.

821 [56] S. Triwahyono, T, Yamada, H. Hattori, Appl. Catal., A 2003, 242, 101-109.

822 [57] A. Gervasini, S. Bennici, Appl. Catal. A-Gen.281 (1-2) (2005) 199-205.

823 [58] Z. Liu, M. Amiridis, Y. Chen, J. Phys. Chem. B. 109 (3) (2005) 1251-1255.

824 [59] A. Y. Yin, J. W. Qu, X. Y. Guo, W. L. Dai, K. N. Fan, Appl. Catal. A, 400 (2011) 39–
825 47.

826 [60] I.C. Freitas, S. Damyanova, D.C. Oliveira, C.M.P. Marques, J.M.C Bueno, Journal of
827 Molecular Catalysis A: Chemical 381 (2014) 26-37.

828 [61] Y. Chen, L. Dong, Y. Jin, X. Bing, J. Weijie, Stud. Surf. Sci. Catal., 101, (1996) 1293-
829 1302.

830 [62] F. Severino, J. Brito, O. Carias, J. Laine, J. Catal., 102 (1) (1986) 172-179.

831 [63] G. Aguila, F. Gracia, J. Cortés, P. Araya, Appl. Catal. B-Environ. 77(3-4) (2008) 325-
832 338.

833 [64] M. Manzoli, R. Di Monte, F. Boccuzzi, S. Coluccia, J. Kaspar, Appl. Catal. B. 61 (3-4)
834 (2005) 192-205.

835 [65] S. Velu, K. Suzuki, C. Gopinath, H. Yoshida, T. Hattori, Phys. Chem. Chem. Phys. 4
836 (10) (2002) 1990-1999.

837 [66] W. Suprun, M. Lutecki, T. Haber, H. Papp, Journal Molecular Catalysis A: Chemical
838 309 (2009) 71-78.

839 [67] J. Ten Dam, U. Hanefeld, ChemSusChem 4 (10) (2011) 1017-1034.

840   [68] J. Agrell, H. Birgersson, M. Boutonnet, I. M. Cabrera, R. Navarro, J.L.G. Fierro, J. Catal.

841   219 (2) (2003) 389-403.

842

843

844

845

846

847